Quantitative evaluation technique of Polyvinyl Alcohol (PVA) fiber dispersion in engineered cementitious composites

Bang Yeon Lee [a], Jin-Keun Kim [a], Jeong-Su Kim [a], Yun Yong Kim [b],*

[a] Department of Civil and Environmental Engineering, Korea Advanced Institute of Science and Technology, 335 Gwahangno, Yuseong-gu, Daejeon 305-701, Republic of Korea
[b] Department of Civil Engineering, Chungnam National University, 220 Gung-dong, Yuseong-gu, Daejeon 305-764, Republic of Korea

ABSTRACT

The fiber dispersion in fiber-reinforced cementitious composites is a crucial factor with respect to achieving desired mechanical performance. However, evaluation of the fiber dispersion in the composite Polyvinyl Alcohol-Engineered Cementitious Composite (PVA-ECC) is extremely challenging because of the low contrast of PVA fibers with the cement-based matrix. In the present work, a new evaluation technique is developed and demonstrated. Using a fluorescence technique on PVA-ECC, PVA fibers are observed as green dots in the cutting plane of the composite. After capturing the fluorescence image with a Charged Couple Device (CCD) camera through a microscope, the fiber dispersion is evaluated using image processing and statistical tools. In the image processing step, the fibers are more accurately detected by employing a series of processes based on categorization, watershed segmentation, and morphological reconstruction. Test results showed that the dispersion coefficient α_f was calculated reasonably and the fiber-detection performance was enhanced.

1. Introduction

Synthetic fibers have been used to improve the toughness of quasi-brittle cement-based materials such as concrete and mortar [1]. Recently developed ultra-ductile Engineered Cementitious Composite (ECC) is an example of application of this approach [2–4]. ECC is a micromechanically designed cementitious composite that is able to exhibit extreme tensile strain capacity (typically more than 2%) while requiring only a moderate amount of fibers (typically less than 2% in a volume fraction). Since the fibers can bridge micro-cracks, the dispersion of fibers strongly influences the resulting mechanical performance of the composite [5].

Several techniques, including image analysis and transmission X-ray photography [6–10], are available for evaluating the fiber dispersion in a composite, i.e., determining the degree to which the fibers are homogeneously dispersed in the composite. These are mostly applicable to non-organic fibers such as steel or glass fibers. Recently, Ozyurt et al. [11,12] proposed a nondestructive technique using AC-impedance spectroscopy and correlated the fiber dispersion, rheology and mechanical performance of FRCs; however, this approach is useful only for conductive fibers including steel and carbon fibers.

To date, the evaluation of organic/non-conducting fiber dispersions has seen little attention. The key step in evaluating an organic fiber dispersion is the fiber detection, since the contrast of organic fibers with cementitious materials is too low to allow detection in the composite by X-ray imaging. To overcome this obstacle, a fluorescence technique has been employed to specifically detect (Polyvinyl Alcohol) PVA fibers using their fluorescent characteristics.

Torigoe et al. [5] suggested a new evaluation technique for PVA fiber dispersions. After capturing a fluorescence image with a Charged Couple Device (CCD) camera through a microscope, the image is divided into small units of appropriate pixel size. The degree of fiber dispersion is then calculated based on the deviation from the average number of fibers in a unit, which is obtained by a rigorous process of directly counting the fibers point by point. In addition, the distribution coefficient, which represents the degree of fiber dispersion, significantly depends on the size of the unit.

In the present work, the authors describe a new image processing technique to eliminate the undesirable impact of the unit size on the distribution coefficient. In the development of the proposed technique, the fiber-detection performance is enhanced by employing categorization, a watershed algorithm, and morphological reconstruction. To categorize the types of fibers, features based on the shape of the fiber image are extracted and a classifier is constructed using an artificial neural network. Then, aggregate fibers are correctly detected using a watershed segmentation algorithm and morphological reconstruction algorithm.

2. Fiber dispersion evaluation technique

The proposed technique is essentially composed of stepwise tasks. First, the specimen is prepared and treated, followed by

* Corresponding author. Tel.: +82 42 821 7004; fax: +82 42 825 0318.
  E-mail address: yunkim@cnu.ac.kr (Y.Y. Kim).

acquisition of a fluorescence image. Based on the proposed image processing algorithm, the fiber images are then automatically detected in a binary image, which is originally converted from the fluorescence image. Next, a mathematical treatment is performed on the data obtained from the previous task, which finally provides the calculated fiber dispersion coefficient of the composite.

2.1. Specimen preparation and image acquisition

The PVA-ECC specimen was produced and then cured in water at $20 \pm 3\,°C$ for 28 days. The specimen was cut with a diamond saw to obtain samples for fiber dispersion evaluation. Each sample, a rectangular block with a size of $13 \times 36 \times 20$ mm in Fig. 1, was polished to create a smooth surface on the exposed cross-section, i.e., the cutting plane. The polished surface was then photographed using image acquisition equipment, i.e., a fluorescence microscope (Olympus, BX51), a CCD camera, and image processing software (Fig. 2). To obtain a digital image, the sample surface was first illuminated by a mercury lamp, followed by capture of a fluorescent image using a CCD digital camera through a Green Fluorescent Protein (GFP) filter under $40\times$ magnification. Fig. 3 shows a fluorescence image of the cutting plane, where greenish points represent PVA fibers.

2.2. Image processing for evaluation of fiber dispersion (proto-type process)

As described in the previous section, the greenish points represent PVA fibers in the fluorescence image. The PVA fibers, there-
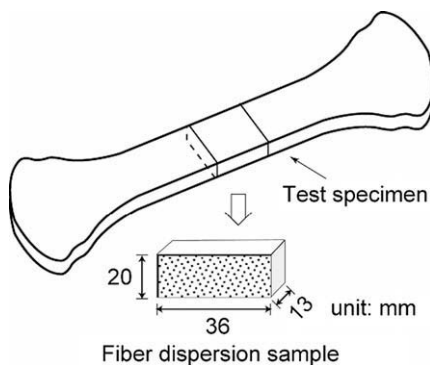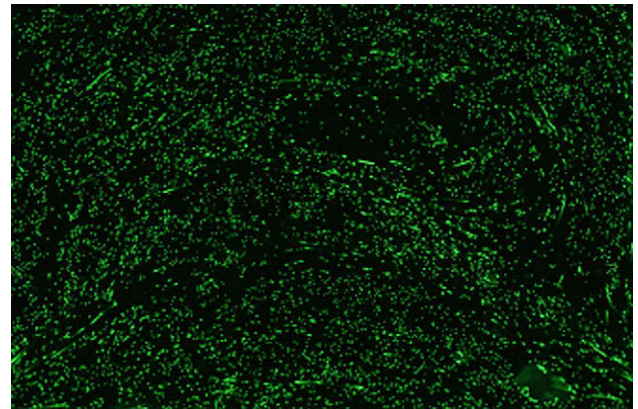

Fig. 3. Fluorescence image.

fore, should be easily detected by segmentation from the background image. The degree of fiber dispersion is then quantitatively evaluated based on calculation of a distribution coefficient α_f, referred to as the fiber dispersion coefficient, as expressed by Eq. (1) as follows [13]:

$$\alpha_f = \exp\left[-\sqrt{\frac{\sum(x_i - 1)^2}{n}}\right] \qquad (1)$$

where n is the total number of fibers on the image and x_i denotes the number of fibers in the ith unit, which is a square portion allocated to the ith fiber on the assumption that the fiber dispersion is perfectly homogeneous. The fiber dispersion coefficient α_f is automatically calculated via the following steps:

(1) Convert the RGB image to a grayscale image.
(2) Convert the grayscale image to a binary image based on a set threshold – object detection based on a thresholding algorithm [14].
(3) Divide the binary image into units, i.e., equivalent squares, of which the total number equals the number of fibers (n).
(4) Obtain the coordinate data for the centroid of each fiber image.
(5) Count the number of fibers (x) located in each unit.

Fig. 1. Sample for the evaluation of fiber dispersion.
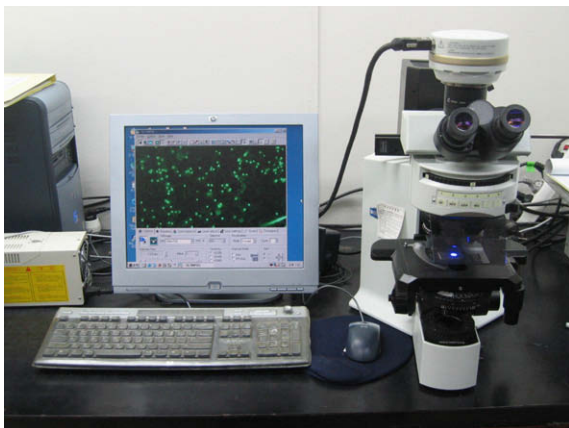
Fig. 2. Fluorescence microscope employed for obtaining fluorescence image (Olympus, BX51).
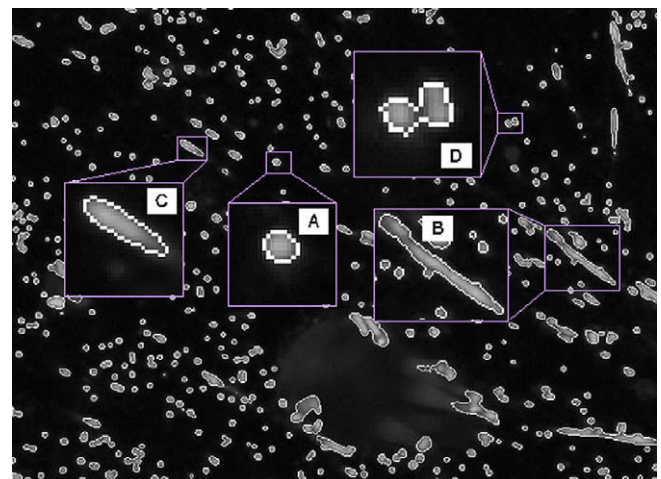

Fig. 4. Composite image obtained by combining original grayscale image with detected binary image (the white line surrounding gray particles).

Following the initial two steps of the image processing, a composite image (Fig. 4) can be obtained by combining the original grayscale image with the detected binary image. As indicated in Fig. 4, fiber images of A–C show quite different shapes in terms of aspect ratio, i.e., length-to-width ratio. This is attributed to the angle created between the fiber orientation and the sawed plane of the sample. In addition, the fiber images of B and D in Fig. 4 reveal a single fiber whereas in reality it is composed of several fibers in close proximity; therefore, further improvement needs to be made to this thresholding algorithm in order to obtain a more accurate dispersion coefficient.

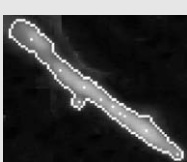## 3. Image processing for enhancing fiber-detection performance

As discussed in the previous section, some improvements need to be made regarding the fiber-detection performance of the proto-type process to detect aggregate fiber images correctly. To this end, an additional process was developed and inserted between step (2) and step (3) (described in the previous section). The added process basically consists of two parts. In the first part, fiber images are categorized into correctly detected single fiber images and aggregate fiber images, which are subdivided into several types, dependent on the shape of image. In the second step, aggregate fiber images are divided into individual fiber images using morphological reconstruction and watershed segmentation.

3.1. Categorization of fiber images

3.1.1. Type of fiber images

The first process entails categorizing fiber images into correctly detected single fibers and potentially aggregate fibers detected as a single fiber. In this process, we employed a watershed segmentation algorithm [15] (see Section 3.2.1) to examine whether a single fiber image detected by the proto-type thresholding algorithm exhibits one segmented object, i.e., a single fiber. Table 1 compares the number of segmented objects with the number of fibers that are obtained from the thresholding algorithm and observations of the fluorescence image. If an image shows a single segmented object, the image is classified as a 'Single fiber,' denoted as Type S1. The fiber images categorized into Type S1 are correctly detected images; therefore, an additional process is not necessary.

Other types of fiber images correspond to cases where the number of objects segmented by the watershed algorithm is more than two. Typical fiber images are classified into four types, i.e., N1 (or S1), N2, N3, and N4, as illustrated in Fig. 5. Four-type categorization, denoted as 1, 2, 3 and 4, is basically established according to the shape characteristics of the image.

Type N1 and Type N2 represent single fiber images that are incorrectly over-segmented [16] by the watershed algorithm, while these fibers are most likely single fibers based on close observation of the fluorescence image. Therefore, an additional process (i.e., beyond the proto-type algorithm) is not required for these two types of fiber images. In terms of the object's shape, Type N1 represents single fiber images whose shape is roughly circular. In contrast, Type N2 includes images of single fibers oriented at roughly right angles to the cutting plane; therefore, these appear highly elongated.

On the other hand, Type N3 and Type N4 represent aggregate fiber images incorrectly detected as a single fiber by the thresholding algorithm. Type N3 mainly corresponds to simply aggregated fibers; thus, they are incorrectly detected as a single fiber. Type N4 represents aggregate fiber images lined up in succession and oriented at diverse angles to the cutting plane; therefore, they are easily over-segmented because of regional minima and maxima in the watershed segmentation process.

3.1.2. Feature selection and database

The second process entails feature extraction. The potential features in images include color, texture, shape, and position of the objects. The shape is the most useful feature for classifying the fiber images since the other features, i.e., color, texture, and position, are not suitable due to undistinguishable color/texture between objects and meaningless position of an object. The shape feature should be invariant to irrelevant transformations such as translation, scaling, rotation, and illumination change. We employed basic shape descriptors, such as object area (A_{ob}), convex hull area (A_{ch}) [17], circumscribed circle area (A_{cc}), perimeter (l_p), and major axis length (l_l) of the object. However, direct use of these descriptors is not appropriate since these are not invariant to scaling, while they are invariant to translation and rotation. Therefore, five descriptors invariant to translation, rotation, and scaling are extracted to classify the fiber images into four types.

Table 1
Type of fiber image.

Type		Number of fibers (thresholding algorithm)	Number of segmented objects (watershed algorithm)	Most probable number of fibers[a]	Example
Single fiber	Type S1	1	1	1	
Possible single fiber	Type N1	1	More than 2	1	
	Type N2	1	More than 2	1	
	Type N3	1	More than 2	More than 2	
	Type N4	1	More than 2	More than 2	

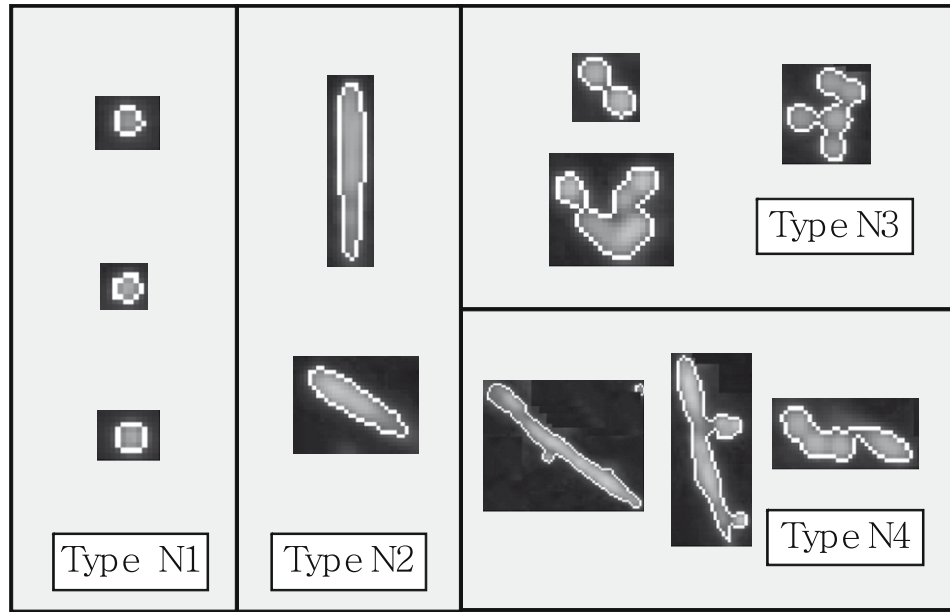[a] These numbers are obtained from fluorescence image observations.

Fig. 5. Typical fiber images according to fiber image types.

The first feature is solidity F_s, which is defined as the division of an object's area by that of the convex hull of an object, as expressed by Eq. (2). This feature can be used to effectively distinguish Type N1 and Type N2 fibers from other types.

$$F_s = \frac{A_{ob}}{A_{ch}} \qquad (2)$$

The second feature is packing density F_c, which is defined as the division of an object's area by that of the object's circumscribed circle, as expressed by Eq. (3). This feature implies how circular the object is, effectively distinguishing Type N1 from others.

$$F_c = \frac{A_{ob}}{A_{cc}} \qquad (3)$$

The value for F_c tends toward 0 for an extremely elongated object, or 1 for a circular object.

F_c is also useful for calculating the inclined angle of the fiber to the cutting plane (Fig. 6), as expressed by Eq. (4).

$$F_c = \frac{\pi dl/4}{\pi l^2/4} = \frac{d}{l} = \frac{d}{d/\cos\theta} = \cos\theta \qquad (4)$$

where θ, d, and l are the inclined angle of the fiber, the diameter of the fiber, and the major axis length of the fiber image, respectively.

The third feature is F_p, which is defined as the division of an object's perimeter by its area, as expressed by Eq. (5). This feature can be used to effectively distinguish Type N3 from the other types.

$$F_p = \frac{l_p}{A_{ob}} \qquad (5)$$

The other features are F_l and F_{rl}, which are defined as the division of the major axis length of the object by A_{ob} and l_{avg} (average value of all the major axis lengths of all fiber images), as expressed by Eqs. (6) and (7), respectively. These features (F_l and F_{rl}) are useful for distinguishing elongated objects (Type N2 and Type N4) from others.

$$F_l = \frac{l_l}{A_{ob}} \qquad (6)$$

$$F_{rl} = \frac{l_l}{l_{avg}} \qquad (7)$$

The database was constructed based on features calculated from 1350 fiber images and used to train an artificial neural network.

3.1.3. Artificial neural network for classification

Artificial neural networks are interconnected groups of artificial neurons that use a mathematical model for information processing based on a connectionist approach to computation. Thus, information or knowledge is represented by massive cross-weighted interconnections through training with a given database.

If artificial neural networks have not been trained concurrently or use an unchangeable database, their architecture can be optimized according to the given database representing a type of
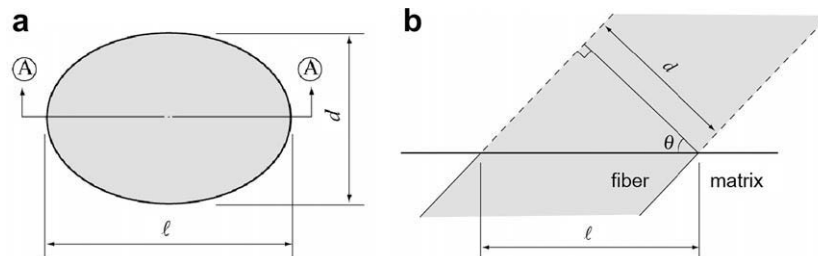

Fig. 6. Basic dimensions of inclined fiber; (a) plan view on the cutting plane; and (b) side view at the section of A-A.

knowledge, so called "knowledge-based structuring". The capability of solving problems of artificial neural networks is determined by the complexity of the networks, which in turn may be determined by the number of layers, the complexity of neurons, the dynamic range of interconnections (weights and biases), and the

Table 2
Desired outputs for training an ANN.

Output node	Type N1	Type N2	Type N3	Type N4
1	1	0	0	0
2	0	1	0	0
3	0	0	1	0
4	0	0	0	1
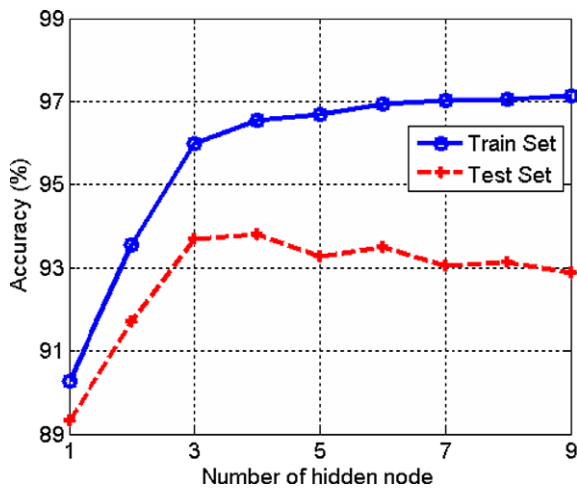
Fig. 7. Performance on the training sets and test sets versus number of hidden nodes.

Table 3
Performance of the classifier, ANN.

Actual classification	ANN classification					Accuracy (%)	
	Type 1	Type 2	Type 3	Type 4	Total		
Type N1	378	0	9	0	387	97.7	95.3
Type N2	1	35	0	3	39	89.7	
Type N3	11	3	822	11	847	97.0	
Type N4	0	1	24	52	77	67.5	

number of hidden nodes. In general, the optimum architecture of an artificial neural network is realized by matching the complexity of the neural network to the complexity of the problem. That is, the architecture of the artificial neural network should be as simple as possible while retaining the capability of solving a given problem. This corresponds with the principle of "Ockam's Razor".

Hecht-Nielsen [18] and Barron [19] provide a proof that one hidden layer of neurons (operating sigmoidal activation functions) is sufficient to model any solution surface of practical interest. Therefore, one hidden layer is used in this study. Moody and Yarvin [20] have compared the performance of several transfer functions and concluded that the sigmoidal transfer functions performed better than other functions, particularly when the data were noisy and contained non-linear relationships. Therefore, the hyperbolic tangent sigmoid function and the linear function are used as transfer functions on hidden neurons and output neurons, respectively (see Eqs. (8) and (9)).

$$f(x) = \frac{2}{1 + e^{-2x}} - 1 \tag{8}$$

$$f(x) = x \tag{9}$$

Weights and biases are determined automatically by the training process. The Levenberg–Marquardt algorithm with weight decay [21] is adopted as a learning algorithm in order to prevent over-fitting. From this learning algorithm, the error function may be expressed by

$$E(\mathbf{w}) = \varepsilon(\mathbf{w}) + \frac{\lambda}{2} \cdot \|\mathbf{w}_{\text{new}} - \mathbf{w}_{\text{old}}\|^2 + \frac{\alpha}{2} \cdot \|\mathbf{w}_{\text{new}}\|^2 \tag{10}$$

where λ and α are the damping parameter and the regularization parameter, respectively. $\mathbf{w}_{\text{new}}$ and $\mathbf{w}_{\text{old}}$ are new and current weight vectors including bias. The role of the second term of Eq. (10) is to keep the step size small so as to ensure that the linear approximation remains valid. The third term is the weight decay term and the first term implying the 1st order approximation of error is expressed by Eq. (11)

$$\varepsilon(\mathbf{w}) = \frac{1}{2} \|\mathbf{T} - \mathbf{Y} + \mathbf{Z} \cdot (\mathbf{w}_{\text{new}} - \mathbf{w}_{\text{old}})\|^2 \tag{11}$$

where $\mathbf{T}$ and $\mathbf{Y}$ are the target vector and the network output vector, respectively, and $\mathbf{Z}$ is a Jacobian matrix that contains the first derivatives of the network errors with respect to the weights and biases. In a back-propagation network, the error at the output neurons is propagated backward to the hidden layer neurons, and then to the input layer neurons, by modifying the connection weights and the biases between them. The modified weights and the biases are expressed by Eq. (12).
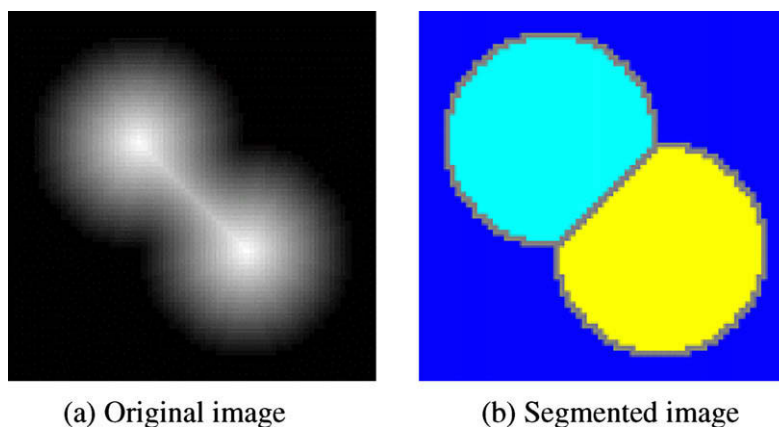
Fig. 8. Watershed segmentation for (a) original image and (b) resulting segmented image.
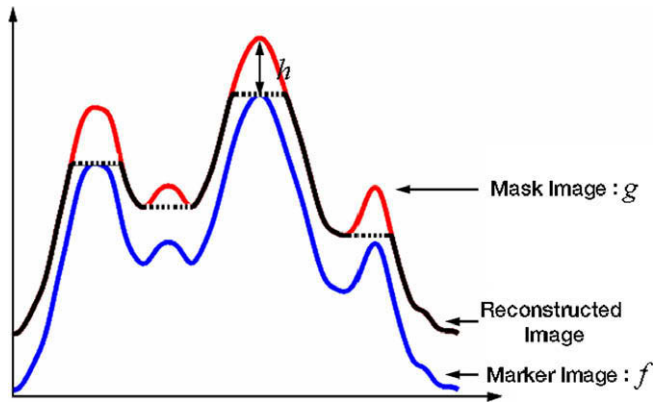
Fig. 9. Morphological reconstruction to minimize over-segmentation in detection of a Type 3 fiber image.

$$\mathbf{w}_{new} = \mathbf{w}_{old} - [\mathbf{Z}^T\mathbf{Z} + \mathbf{I}(\lambda + \alpha)]^{-1} \cdot [\mathbf{Z}^T\varepsilon(\mathbf{w}) + \alpha \cdot \mathbf{w}_{old}] \quad (12)$$

where $\mathbf{I}$ is the identity matrix.

In order to determine the number of hidden nodes, a 10-fold cross-validation method is adopted, wherein networks having different numbers of hidden nodes are trained. The network having the best performance, that is, the case where the accuracy on the test sets is the maximum, is then selected. This process is repeated 10 times so as to minimize the effect of the initial values of weights and biases for each fold data set. Five features are used as input parameters, and the desired outputs for learning are given in Table 2. Fig. 7 shows the accuracy on the training sets and test sets versus the number of hidden nodes. The optimum network architecture is accordingly found to be 5-4-4 (number of neurons in input layer, 5;

number of neurons in hidden layer, 4; and number of neurons in output layer, 4); i.e., this architecture yielded the maximum accuracy on the test sets. The artificial neural network that will be used for the classification of fiber images is trained using the whole database. The accuracy of the artificial neural network on the basis of a jack-knife validation is 95.3% (Table 3). The artificial neural network constructed in this study is presented in the Appendix, and it can be used to classify the types of fiber image.

3.2. Detection of aggregate fiber images (Type N3 and Type N4)

In order to correctly detect an aggregate fiber image (Type N3 and Type N4), a watershed segmentation algorithm and morphological reconstruction algorithm were employed in the present study.

3.2.1. Watershed segmentation

To correctly detect Type N3 and Type N4, a watershed segmentation algorithm was adopted. Digabel and Lantuéjoul [22] introduced watershed segmentation as a morphological tool. Beucher and Lantuéjoul [23] improved this original algorithm to extend it to a more general framework of grayscale images. Fig. 8 shows an example of watershed segmentation. Currently, watershed transformation is a widely used technology in image segmentation. Its basic concept derives from the concepts of catchment basins and watershed from topography [24]. Watershed segmentation can be implemented on the basis of an immersion analogy. The immersion analogy concept is based on an analogy that all points on a surface are classified according to filling and merging the catchment basins from the bottom. The water starts filling all
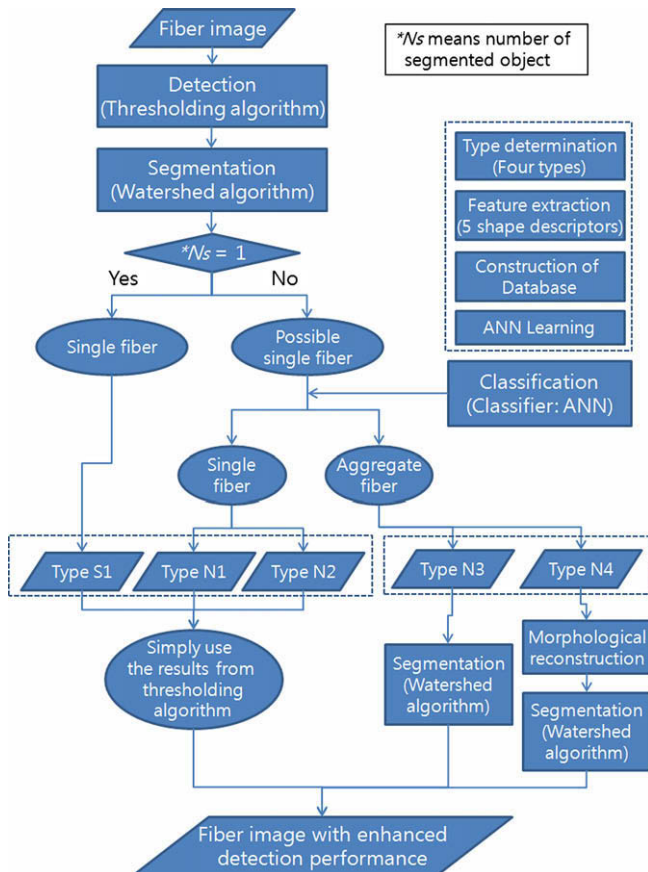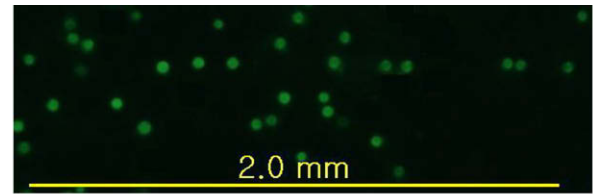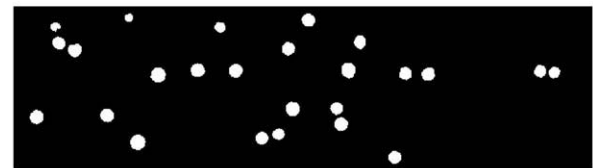

Fig. 10. Flow chart of enhanced detection algorithm.

(a) Original fiber image

(b) Detected fiber image
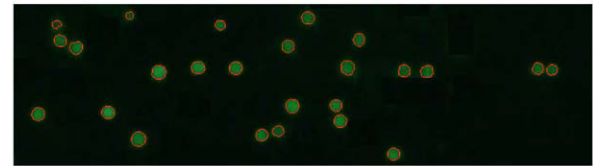
(c) Composite image in which the red line surrounding the green fiber image is the outline of the detected fiber image

Fig. 11. Composite image obtained by combining original fluorescence image with detected fiber image.

Table 4
Diameter of fiber image, which is equivalent to the minor axis length.

	Real	Test 1	Test 2	Average	Error (%)
Diameter of fiber (μm)	39.5	42.1	42.3	42.2	6.84

catchment basins. If two catchment basins are about to merge, a high dam is built to prevent this. When all basins have been filled, the dams represent the watershed lines. In this study, a watershed segmentation algorithm based on the immersion analogy proposed by Vincent and Soille [15] was adopted.

3.2.2. Morphological reconstruction

Morphological reconstruction is adopted to minimize the over-segmentation problem caused by regional minima and maxima in

Fig. 12. Grayscale image to assess the performance of the enhanced detection process and seven groups of fiber images selected for close examination.

the watershed segmentation process of Type N4. In the standard morphological reconstruction, a mask image (g) is reconstructed from a marker image (f) by iterating geodesic dilations of the marker image inside the mask image until stability is attained; i.e., the image no longer changes. Both of these images have the same size, and $f \leqslant g$ [25]. Fig. 9 illustrates the concept of a reconstructed image. A mask image is the initial image that will be reconstructed and a marker image is created by subtracting a constant value (h) from the mask image. The number of fibers finally detected from Type N4 fibers is dependent on the value of h. In this study, h was determined to be 20, empirically by the use of trial and error.

Fig. 10 shows an elaborate diagram of the components and process of the enhanced detection process. First, we examine whether a single fiber image, detected by the proto-type procedure (thresholding algorithm), exhibits one segmented object, i.e., a single fiber, by the use of the watershed segmentation algorithm. The fibers are then classified into two categories, single fibers (Type S1) and possible single fibers (Type N family). Next, the fibers in Type N family are subdivided into four types (Types N1, N2, N3 and N4) by the ANN. Finally, more accurate detection of Type N3 is achieved by applying the watershed segmentation algorithm, while morphological reconstruction is performed on Type N4 for the purpose of relieving the over-segmentation problem, followed by watershed segmentation.

4. Validation of the method

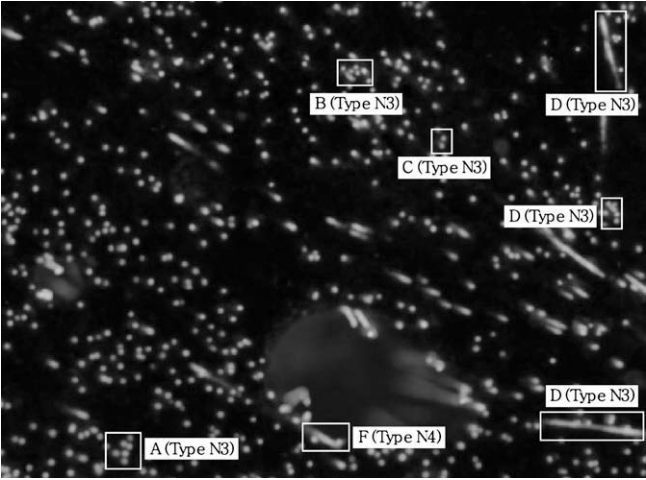To assess the validity of the proposed technique, a series of tests was performed on real and artificial fiber images.
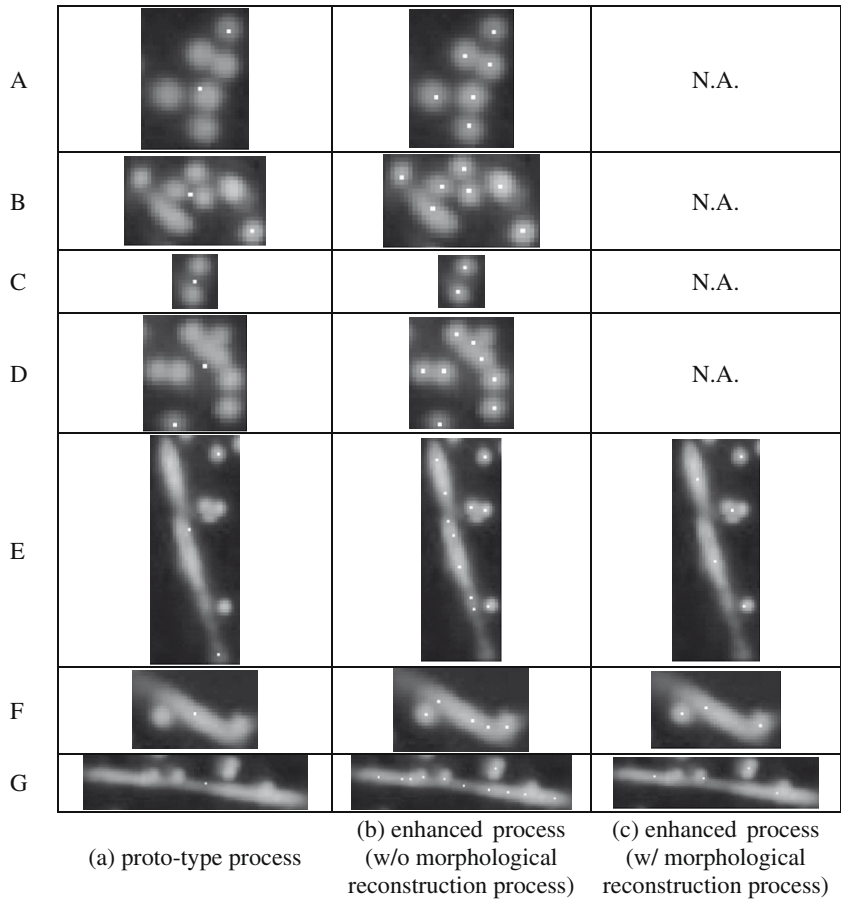

Fig. 13. Test results, where the white point located on the grayscale image (fiber) indicates the center of the detected fiber image.

4.1. Diameter of detected fiber images

The diameters of the detected fiber images are compared with the nominal diameter of the fiber to examine the accuracy of the proposed technique. The minor axis length of the object can be simply taken as the diameter of the fiber. Fig. 11 shows the original fluorescence image, the detected fiber image, and the composite image obtained by combining the original fiber image with the detected fiber image. Comparison results are listed in Table 4. The fiber diameter, i.e., the minor axis length, is estimated to be 6.84% larger than the nominal diameter of the fiber. This discrepancy is most likely due to the lower threshold value used to distinguish object pixels from background pixels. The size of the fiber image is not crucial for evaluating the fiber dispersion performance;
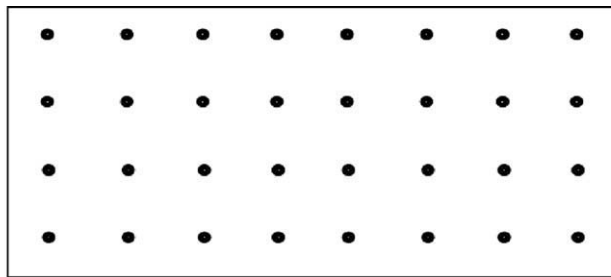
therefore, 6.84% error appears to be tolerable in the present study. However, in the event that it is determined that the fiber size is indeed an important factor, an optimal threshold value should be determined.

4.2. Fiber-detection performance

Fig. 12 shows the grayscale image tested in order to assess the performance of the enhanced detection process and seven groups of fiber images were selected for closer examination. Fig. 13 displays the detection test results, where the white point located on the grayscale image (fiber) indicates the center of the detected fiber image. A–D fiber images in Fig. 13, which were classified as Type N3 fibers, were more successfully detected using the enhanced detection process relative to the results of the proto-type process. Detection results of E–G fiber images (Type N4) in Fig. 13 are also indicative of significantly improved fiber-detection performance, where over-segmentation is minimized by applying the morphological reconstruction. All results in Fig. 13(c) indicate that the enhanced detection process yields significantly improved fiber-detection performance.

4.3. Calculation of fiber dispersion coefficient (α_f)

Fig. 14, in which the dispersions of (a) and (b) are perfect and severely biased, respectively, shows artificial fiber images tested to assess the validity of the α_f calculation. The proposed method showed α_f values of 1.0 and 0.041 for each image (see Fig. 14). This means that the correct calculations of α_f values were demonstrated. Table 5 compares α_f values calculated by the proto-type algorithm and the enhanced algorithms for the whole fiber image detected from fluorescence photograph and seven parts of that, which are seven groups of fiber images selected for close examination (Fig. 12). As shown in Table 5, the enhanced algorithm without a morphological reconstruction process provides lower α_f values, e.g. a decrease of 11.5% for a whole fiber image, compared to the proto-type algorithm. This is most likely due to correct segmentation of the fibers from the aggregate fiber images, where the fibers are located in close enough proximity to decrease the average α_f for the same sample. On the other hand, the enhanced algorithm with a morphological reconstruction process that minimizes over-segmentation provides higher α_f values, e.g. an increase of 2.35% for a whole fiber image, compared to the enhanced algorithm without

(a) artificial fiber image with perfect dispersion, α_f=1.0

(b) artificial fiber image with severely biased dispersion, α_f=0.041

Fig. 14. Artificial fiber images to test.

Table 5
α_f Values calculated by proto-type and enhanced processes.

Fiber image		(a) Proto-type process	(b) Enhanced process (w/o morphological reconstruction process)	(c) Enhanced process (w/morphological reconstruction process)
A	α_f	1	0.368	NA
	Number of fibers	2	6	NA
B	α_f	1	0.430	NA
	Number of fibers	2	7	NA
C	α_f	1	1	NA
	Number of fibers	1	2	NA
D	α_f	1	0.493	NA
	Number of fibers	1	8	NA
E	α_f	1	0.450	0.665
	Number of fibers	3	11	5
F	α_f	1	0.531	1
	Number of fibers	1	5	3
G	α_f	1	0.466	1
	Number of fibers	1	11	4
Whole fiber image	α_f	0.384	0.340	0.348
	Number of fibers	480	635	565

a morphological reconstruction process. This is most likely due to correct segmentation of the fibers from the Type N4 fiber images, where the closely over-segmented fibers are removed, leading to an increased average α_f for the same sample. The image processing technique proposed in this study will be potentially applied to assess the impact of the fiber distribution, such as the orientation, number, and dispersion of fibers on the mechanical properties, i.e., fiber bridging constitutive law, of PVA-ECC, details of which will be presented in a follow–up paper.

5. Conclusions

This paper proposes a new technique to evaluate the PVA fiber dispersion in Engineered Cementitious Composites. The proposed technique is expected to be useful in assessing the impact of the fiber distribution on the mechanical properties of fiber-reinforced cement composites. A series of experimental and analytical investigations was carried out to assess the validity of this technique. The following conclusions can be drawn from the current results:

(1) The proposed technique is essentially composed of four tasks, i.e., specimen preparation, image acquisition, image processing for fiber detection, and mathematical treatment for calculation of fiber dispersion coefficient. In the development of proposed technique, an enhanced fiber detection algorithm based on categorization, watershed algorithm, and morphological reconstruction are also proposed to enhance the fiber-detection performance.
(2) The fiber diameter calculated by the proposed technique is 6.84% larger than the nominal diameter of the fiber. This was deemed tolerable in the present study since the size of the fiber image is relatively unimportant for evaluating the fiber dispersion.
(3) The calculation accuracy of fiber dispersion coefficient α_f was demonstrated by tests on artificial fiber images. In addition, the results of real fiber image tests indicated significant improvement of the fiber-detection performance. This was achieved by applying an enhanced detection algorithm, correctly separating fiber images from the aggregate image, and relieving the over-segmentation problem.

Acknowledgements

Appendix A

The artificial neural network described below can provide the classification of the fiber images as an output. If the ith output node shows a maximum value among four output nodes, the type of fiber image is determined as the ith type.

$$\mathbf{y}(\mathbf{x}) = \mathbf{\Omega} \cdot \mathbf{f}_{\text{tansig}}(\mathbf{W} \cdot \mathbf{x} + \mathbf{b}) + \mathbf{\beta} \tag{A.1}$$

where $\mathbf{W}$ and $\mathbf{\Omega}$ are weight matrices for input and hidden nodes, respectively. $\mathbf{b}$ and $\mathbf{\beta}$ are bias vectors for input and hidden nodes, respectively. $\mathbf{W}$, $\mathbf{b}$, $\mathbf{\Omega}$, and $\mathbf{\beta}$ values are given in (A.2)–(A.5).

$$\mathbf{W} = \begin{bmatrix} 1.6297 & -7.7593 & 0.31364 & -2.0195 & -0.46188 \\ -1.8128 & 8.6413 & 2.3222 & 0.94749 & 1.7942 \\ -9.4296 & -2.3026 & -3.1304 & 5.6831 & 11.7617 \\ 7.1932 & -8.4463 & -13.8043 & 4.2301 & -1.7733 \end{bmatrix} \tag{A.2}$$

$$\mathbf{b} = \begin{bmatrix} -4.9751 \\ 7.4258 \\ 19.1946 \\ -9.7944 \end{bmatrix} \tag{A.3}$$

$$\mathbf{\Omega} = \begin{bmatrix} 0.015847 & 0.026829 & -1.0049 & 0.020441 \\ 0.04508 & 0.088457 & -0.00939 & 1.0427 \\ -1.4036 & -0.94918 & 1.0114 & -0.47177 \\ 1.3426 & 0.83375 & 0.002828 & -0.5913 \end{bmatrix} \tag{A.4}$$

$$\mathbf{\beta} = \begin{bmatrix} 0.004288 \\ 0.003137 \\ -0.92934 \\ -1.0779 \end{bmatrix} \tag{A.5}$$

In Eq. (A.1), the input nodes should be treated with transformed values from -1 to $+1$ using a linear mapping function (A.6), i.e., $\mathbf{x} = \mathbf{f}_{\text{mapping}}(\langle F_s\ F_c\ F_p\ F_l\ F_{rl}\rangle^{\text{T}})$. In Eq. (A.6), the minimum ($t_{i,\min}$) and the maximum ($t_{i,\max}$) values for transforming inputs are as follows: $\min(F_s\ F_c\ F_p\ F_l\ F_{rl}) = (0.3913, 0.028, 0.2461, 0.0512, 0.3996)$ and $\max(F_s\ F_c\ F_p\ F_l\ F_{rl}) = (1, 0.962, 1.0365, 0.4538, 10.532)$. In addition, the hyperbolic tangent sigmoid function and the linear function as transfer functions on hidden neurons and output neurons are given in Eq. (A.7) and Eq. (A.8).

$$\mathbf{f}_{\text{mapping}}(\mathbf{t}) = \left\langle \frac{2(t_1 - t_{1,\min})}{t_{1,\max} - t_{1,\min}} - 1 \quad \frac{2(t_2 - t_{2,\min})}{t_{2,\max} - t_{2,\min}} - 1 \quad \cdots \right\rangle^{\text{T}} \tag{A.6}$$

$$\mathbf{f}_{\text{tansig}}(\mathbf{t}) = \left\langle \frac{2}{1 + e^{-2t_1}} - 1 \quad \frac{2}{1 + e^{-2t_2}} - 1 \quad \cdots \right\rangle^{\text{T}} \tag{A.7}$$

$$\mathbf{f}_{\text{purlin}}(\mathbf{t}) = \langle t_1 \quad t_2 \quad \cdots \rangle^{\text{T}} \tag{A.8}$$

References

[1] Li VC, Wang S, Wu C. Tensile strain-hardening behavior of polyvinyl alcohol-engineered cementitious composite (PVA-ECC). ACI Mater J 2001;98(6):483–92.
[2] Li VC. Reflections on the research and development of ECC. In: Proceedings of the JCI international'l workshop on ductile fiber reinforced cementitious composites application and evaluation (DFRCC'2002), Takayama, Japan, October; 2002. p. 1–21.
[3] Kim YY, Kong HJ, Li VC. Design of engineered cementitious composite suitable for wet-mixture shotcreting. ACI Mater J 2003;100(6):511–8.
[4] Kim JK, Kim JS, Ha GJ, Kim YY. Tensile and fiber dispersion performance of ECC (engineered cementitious composites) produced with ground granulated blast furnace slag. Cem Concr Res 2007;37(7):1096–105.
[5] Torigoe S, Horikoshi T, Ogawa A. Study on evaluation method for PVA fiber distribution in engineered cementitious composite. J Adv Concr Technol 2003;1(3):265–8.
[6] Guild FJ, Summerscales J. Microstructural image analysis applied to fibre composites materials: a review. Composites 1993;24(5):383–93.
[7] Yang Y. Methods study on dispersion of fibers in CFRC. Cem Concr Res 2002;32:747–50.
[8] Chermant JL, Chermant L, Coster M, Dequiedt AS, Redon C. Some fields of applications of automatic image analysis in civil engineering. Cem Concr Compos 2001;23:157–69.
[9] Benson SDP, Karihaloo BL. CARDIFRC—manufacture and constitutive behavior. In: High performance fiber reinforced cement composites (HPFRCC4), Ann Arbor. Mich.; 2003. p. 65–79.
[10] Akkaya Y, Shah SP, Ankenman B. Effect of fiber dispersion on multiple cracking of cement composites. J Eng Mater Civil Eng 2001;127(4):311–6.
[11] Ozyurt N, Woo LY, Mason TO, Shah SP. Monitoring fiber dispersion in fiber-reinforced cementitious materials: comparison of AC-impedance spectroscopy and image analysis. ACI Mater J 2006;103(5):340–7.
[12] Ozyurt N, Mason TO, Shah SP. Correlation of fiber dispersion, rheology and mechanical performance of FRCs. Cem Concr Compos 2007;29(2):70–9.
[13] Kobayashi K. Fiber reinforced concrete. Tokyo: Ohm-sha; 1981.
[14] Otsu NA. Threshold selection method from gray level histogram. IEEE Trans Syst Man Cybernet 1979;9(1):62–6.

[15] Vincent L, Soille P. Watersheds in digital spaces: an efficient algorithm based on immersion simulations. IEEE Trans Pattern Anal Machine Intell 1991;13(6):583–98.

[16] Beucher S. The watershed transformation applied to image segmentation. In: Conference on signal and image processing in microscopy and microanalysis, September; 1991. p. 299–314.

[17] Barber CB, Dobkin DP, Huhdanpaa HT. The quickhull algorithm for convex hulls. ACM Trans Math Software 1996;22(4):469–83.

[18] Hecht-Nielsen R. Theory of the backpropogation neural network. In: Proceedings of international joint conference on neural networks, vol. I. Washington (DC, USA): IEEE; 1989. p. 593–605.

[19] Barron AR. Universal approximation bounds for superpositions of a sigmoidal function. IEEE Trans Inform Theory 1993;39(3):930–45.

[20] Moody JE, Yarvin N. Networks with learned unit response functions. In: Moody JE, Hanson SJ, Lippmann RP, editors. Advances in neural information processing systems vol. 4. Morgan Kaufmann Publishers; 1992. p. 1048–55.

[21] Krogh A, Hertz JA. A simple weight decay can improve generalization. In: Moody JE, Hanson SJ, Lippmann RP, editors. Advances in neural information processing systems vol. 4. Morgan Kaufmann Publishers; 1992. p. 950–7.

[22] Digabel H, Lantuéjoul C. Iterative algorithms, In: Chermant JL, editor. Proceedings of the 2nd European symposium on quantitative analysis of microstructures in material science, biology and medicine, Caen, France, October 1977, . Stuttgart, West Germany: Riederer Verlag; 1978. p. 85–99.

[23] Beucher S, Lantuéjoul C. Use of watershed in contour detection. In: International workshop on image processing: real-time edge and motion detection/estimation, Rennes, France; 1979. p. 17–21.

[24] Feng J, Lu H. Peak analysis of grayscale image: algorithm and application. Int J Info Technol 2006;12(5):11–8.

[25] Vincent L. Morphological grayscale reconstruction in image analysis: applications and efficient algorithms. IEEE Trans Image Process 1993;2(2):176–201.